Front. Earth Sci. 2025, 19(3): 341−356
https://doi.org/10.1007/s11707-024-1106-1

RESEARCH ARTICLE

Predictability analysis based on ensemble forecasting of the "7·20" extreme rainstorm in Henan, China

Sai TAN[1], Qiuping WANG[1], Xulin MA (✉)[1], Lu SUN[2,3], Xin ZHANG[1], Xinlu LV[1], Xin SUN (✉)[4]

1 Key Laboratory of Meteorological Disaster (Ministry of Education), Nanjing University of Information Science and Technology, Nanjing 210044, China
2 Meteorological Institute of Shaanxi Province, Xi'an 710016, China
3 Key Laboratory of Eco-Environment and Meteorology for the Qinling Mountains and Loess Plateau, Shaanxi Meteorological Service, Xi'an 710014, China
4 Meteorological Observatory of Inner Mongolia Meteorological Service, Huhhot 010051, China

Abstract A heavy rainstorm occurred in Henan Province, China, between 19 and 21 July, 2021, with a record-breaking 201.9 mm of precipitation in 1 h. To explore the key factors that led to forecasting errors for this extreme rainstorm, as well as the dominant contributor affecting its predictability, we employed the Global/Regional Assimilation and Prediction System-Regional Ensemble Prediction System (GRAPES-REPS) to investigate the impact of the upper tropospheric cold vortex, middle-low vortex, and low-level jet on predictability and forecasting errors. The results showed that heavy rainfall was influenced by the following stable atmospheric circulation systems: subtropical highs, continental highs, and Typhoon In-Fa. Severe convection was caused by abundant water vapor, orographic uplift, and mesoscale vortices. Multiscale weather systems contributed to maintaining extreme rainfall in Henan for a long duration. The prediction ability of the optimal member of GRAPES-REPS was attributed to effective prediction of the intensity and evolution characteristics of the upper tropospheric cold vortex, middle-low vortex, and low-level jet. Conversely, the prediction deviation of unstable and dynamic conditions in the lower level of the worst member led to a decline in the forecast quality of rainfall intensity and its rainfall area. This indicates that heavy rainfall was strongly related to the short-wave throughput, upper tropospheric cold vortex, vortex, and boundary layer jet. Moreover, we observed severe uncertainty in GRAPES-REPS forecasts for rainfall caused by strong convection, whereas the predictability of rainfall caused by topography was high. Compared with the European Centre for Medium-Range Weather Forecasts Ensemble Prediction System, GRAPES-REPS exhibits a better forecast ability for heavy rainfall, with some ensemble members able to better predict extreme precipitation.

Keywords numerical weather prediction, ensemble forecast, ensemble sensitivity, predictability, extreme rainfall

1 Introduction

Numerical forecasting is the most effective method for improving rainstorm prediction accuracy. Catastrophic weather events are often triggered by extreme short-term heavy precipitation, such as torrential rain in Beijing on July 21, 2012 (Sun et al., 2012; Sun et al., 2013) and heavy rainfall in Henan on July 19, 2018 (Li et al., 2018). Thus, the underestimation of precipitation can lead to urban waterlogging, debris flows, flash floods, and other natural disasters, which are likely to cause serious social and economic losses. Moreover, deterministic forecasts have difficulty in meeting the demands of operational forecasting (Gao et al., 2019; Wu et al., 2019).

Thus, based on the dynamic stochastic prediction theory, the Monte Carlo ensemble forecast method (Leith, 1974) was proposed to solve the uncertainty problem of numerical prediction caused by initial errors, model errors, and the chaotic nature of the atmosphere (Melhauser and Zhang, 2012). Compared to deterministic forecasting, ensemble forecasting can effectively and quantitatively represent predictability or reliability, as well as the occurrence probability, providing uncertainty information and other scientific advantages (Lorenz,

Received July 13, 2023; accepted October 4, 2023

E-mails: xulinma@nuist.edu.cn (Xulin MA)
641680001@qq.com (Xin SUN)

1963,1969;Du, 2002;Torn and Hakim, 2008;Schumacher, 2011).

Ensemble forecasting services are being actively developed around the world (Zhang, 2018a, 2018b; Medina et al., 2019; Chen and Li, 2020; Pan et al., 2021). The European Centre for Medium-Range Weather Forecasts ensemble prediction system (ECMWF-EPS) is the best-performing and most widely used service (Yu and Meng, 2016; Du and Chen, 2018; Chen et al., 2019). However, despite a good ability to express synoptic-scale systems, this global ensemble forecast cannot effectively describe the evolution of the convective system. Thus, researchers have attempted to improve the spatial-temporal resolution of high-resolution regional ensemble forecast systems, resulting in an improved precipitation forecasting ability (Ji and Qi, 2018). For example, the Tropical Regional Atmosphere Model for the South China Sea (CMA-TRAMS) provides precipitation forecasts that are closer to actual observations than those of the ECMWF-EPS; however, CMA-TRAMS still exhibits limitations forecasting precipitation extremes (Xiao et al., 2021). Moreover, assessment of the WRF-based Rapid Update Cycle from Beijing Meteorological Bureau (BJ-RUC) revealed poor performance in rainfall intensity forecasting resulting from the imperfect simulation of water vapor and instability conditions (Jiang et al., 2014). Sun et al. (2022) studied the predictability of heavy warm-sector rainfall in south China according to ensemble forecast sensitivity and demonstrated the sensitivity of numerical prediction quality to the initial value of ensemble forecasting. Undoubtedly, ensemble forecasting techniques, especially high-resolution regional ensemble forecasting methods, produce better heavy precipitation forecasts than deterministic forecasting methods (Zhu and Xue, 2016).

The extreme rainstorm process that occurred in Henan Province, China, on July 20, 2022 (hereafter the "7.20" event) was affected by multi-scale and multi-weather systems, and the maximum hourly rainfall reached 201.9 mm, which broke historical records. Such an event poses a significant challenge for operational numerical forecasting (Wei et al., 2023). Although the forecasting capability of the Global/Regional Assimilation and Prediction System-Regional Ensemble Prediction System (GRAPES-REPS) (Xue and Liu, 2007; Ma et al., 2009) is continually being improved (Ma et al., 2018, 2021; Wang et al., 2021; Zhang et al., 2022a), the precipitation intensity forecast for the "7·20" event in Henan was poor, and the system does not effectively meet current requirements.

Many researchers have studied the "7·20" extreme precipitation event from the perspective of its characteristics and circulation anomalies (Zhang et al., 2021), microphysical processes (Chen et al., 2022), water vapor transport, and pivotal synoptic scale systems (Cholaw et al., 2022). Other studies have been conducted on the uncertainty, error growth mechanisms, and convective-scale predictability (Zhang et al., 2022b; Zhu et al., 2022), providing a good scientific basis for understanding this extreme weather event. However, the predictability and physical mechanism of the "7·20" event is still not accurately understood. Therefore, to provide insights into the causes of the observed forecast deviation, we analyzed the physical mechanism, key forecast factors, and predictability of the "7·20" event using GRAPES-REPS. The aims of this study are to enhance our understanding of the predictability of extreme weather using ensemble forecasts, to improve our ability to forecast extreme events, and to provide references for future regional ensemble forecast improvements.

2 Data and method

2.1 Ensemble forecast system and data

The operational regional ensemble forecasting system GRAPES-REPS V3.0 was used in this study. ECMWF-EPS data was used to evaluate the forecasting effects of GRAPES-REPS, starting at 1200 UTC on July 19, 2021. The ensemble forecast system GRAPES-REPS, which was operational in the forecast area (15°N–65°N, 70°E–145°E) during the "7·20" event, consists of 14 ensemble members and a control member with 17 isobaric surface layers, and the probability distribution of prediction error can be described reasonably. The initial conditions were provided by the National Centers for Environmental Prediction Global Forecast System (NCEP-GFS), and the corresponding initial perturbations were generated by the warming-start of the Ensemble Transform Kalman Filter (ETKF) scheme with a 6-h cycle (Ma et al., 2009, 2021; Wang et al., 2021). The LBC (lateral boundary condition) perturbation is derived from the GRAPES-GEPS. That is, extracting the LBC perturbation of the GRAPES-GEPS member to be superimposed on the control member of GRAPES-REPS V3.0. The model perturbation method is a single physical process parameterization scheme and stochastic perturbed parameterization tendencies (SPPT, Buizza et al., 1999; Yuan et al., 2016). Convection Parametric Scheme adopt KF. Boundary Layer Parametric Scheme adopt MRF and YSU.

The ECMWF-EPS has 50 ensemble members and one control member. The results are similar between the 15-member ECMWF-EPS and the 51-member ECMWF-EPS. The 51-member result is shown in this study. The high-resolution precipitation products obtained from the Climate Prediction Center's morphing technique (CMORPH) for July 18−22, 2021 are used to analyze heavy rainfall and ECMWF reanalysis data ERA5, as shown in Table 1.

2.2 Ensemble sensitivity analysis method

Torn and Hakim (2008) proposed an ensemble sensitivity

Table 1 Summary of data

Data type	Name	Description	Horizontal resolution	Temporal resolution
Real data	Rain data	CMORPH	0.05° × 0.05°	1 h
	ERA5	Reanalysis data	0.25° × 0.25°	1 h
Ensemble forecast	GRAPES-REPS	Regional Ensemble Forecast	0.1° × 0.1°	1 h
	ECMWF-EPS	Global Ensemble Forecast	0.5° × 0.5°	6 h

analysis that assumed a linear relationship between the disturbance of the initial field (or the forecast field at a certain time) in the ensemble forecast model at a certain spatial point and its subsequent forecast. By establishing a linear regression equation for the predictor (dependent variable) and initial (or previous time-predicted) disturbance state (independent variable), the slope of the linear regression equation represents the ensemble sensitivity. The ensemble sensitivity S at any predictor J of all members to the disturbance state X_i at the initial time (or the forecast at a certain time) can be expressed as

$$s = \frac{\partial J}{\partial x_i} = \frac{\mathrm{cov}(J, X_i)}{\sqrt{\mathrm{var}(x_i)}}, \tag{1}$$

where the one-dimensional scalar J is the forecast value of all members, the two-dimensional scalar X_i is the state value of all members on the i lattice in the model region, cov represents the covariance between J and X_i, and var represents the variance in the state quantity. Accordingly, the correlation coefficients of J and X_i are proportional to the ensemble sensitivity:

$$\mathrm{cor}(J, x_i) = \frac{\mathrm{cov}(J, x_i)}{\sigma_J \cdot \sigma_{xi}} = s \cdot \sigma_J, \tag{2}$$

where σ_J is the standard deviation of the forecast value.

Because the standard deviation of the predictor (scalar) is fixed at a certain time, the ensemble sensitivity S can be simplified to be expressed by the correlation coefficient. As a dimensionless number, the correlation coefficient reflects the strength of the linear relationship between the state and forecast variables. The greater the absolute value of the ensemble sensitivity S, the more a disturbance of the state variable at the initial time (or at a certain time) can cause a large change in the forecast quantity, indicating that the forecast quantity is more sensitive to the state variable. Compared with the ensemble sensitivity to different state variables, we determined the state variables, weather systems, and ensemble sensitivity regions that have the greatest impact on the forecast (Quandt et al., 2019).

3 The "7·20" Heavy Rainstorm Event

3.1 Observed precipitation

From 1200 UTC July 18 to 1200 UTC July 21, heavy rainfall occurred in northcentral Henan, southeastern Shanxi, and southwestern Hebei along the eastern side of the Taihang Mountains. Heavy rain occurred continuously in central and northern Henan for four days, and the accumulated precipitation in most areas was between 200 mm and 400 mm; the precipitation amount in some cities such as Zhengzhou, Hebi, Xinxiang, and Jiaozuo reached up to 500 mm (Fig. 1(a)). The weather process of this extreme rainstorm event in Henan was mainly reflected in the total precipitation, daily precipitation, and hourly precipitation intensity. The single-station hourly precipitation data showed that the precipitation was most concentrated on 20 July, reaching a peak at approximately 0900 UTC. The precipitation center on July 21 was located in Hebi (Fig. 1(b)). The regional average hourly precipitation showed that the rainy area moved southward from July 18 to 20 then northward from July 20 to 21 (Fig. 1(c)). This extreme rainstorm process was characterized by a long duration, large accumulated rainfall, a wide range of heavy rainfall, and extremely strong short-term rainfall.

3.2 Weather conditions

We analyzed the circulation of heavy precipitation using ERA5 reanalysis data (Fig. 2). A low-trough area was observed at 200 hPa in the upper troposphere in the eastern part of the Ural Mountains, and the South Asian High (with 12560 gpm as its characteristic contour) was located over the Tibetan Plateau, with the characteristic contour extending eastward to 98°E at 1200 UTC on 19 July. A cold vortex existed over the East China Sea, as well as a low trough near the Hetao Plain and a corresponding high-pressure ridge in front of the plain, which affected the Huang-Huai area. From 1200 UTC July 17 to 1200 UTC July 19, the South Asian High retreated west and advanced northeast until 1200 UTC 21 July, and the coastal vortex moved slowly northward. The low trough over the Hetao Plain was less active, and the Huang-Huai area was continuously controlled by a high-pressure ridge. In this evolution process, the typhoons "In-Fa" (No. 2106) and "Cempaka" (No. 2107) developed successively on the sea surface of eastern Taiwan and southern coastal areas (Fig. 2(a)).

At 1200 UTC on 19 July, the lowest trough was located at over 500 hPa in the middle troposphere in northwest Xinjiang. The continental high was located in the

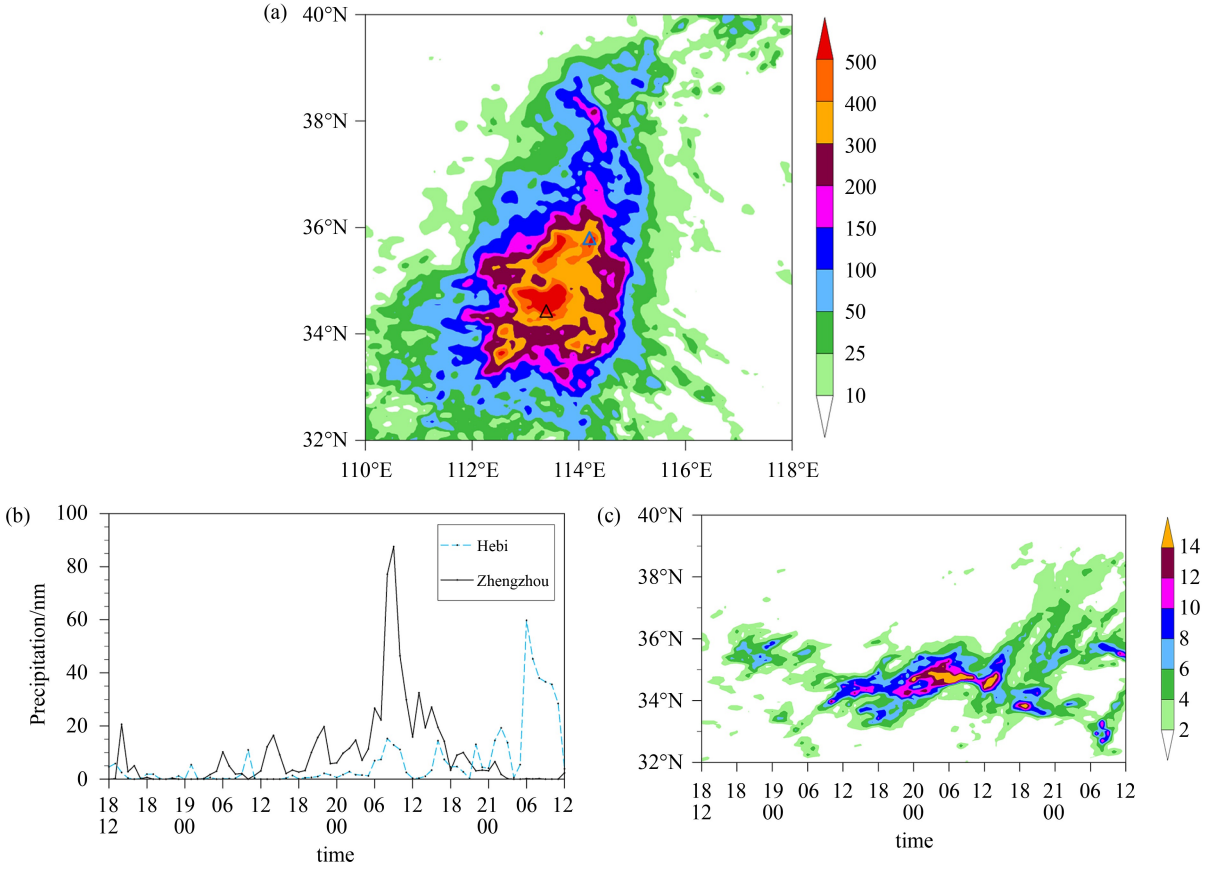

Fig. 1 Observational precipitation (unit: mm) from 1200 UTC on July 18 to 1200 UTC on July 21, 2021. (a) Accumulated precipitation, (b) hourly precipitation at Zhengzhou Station (black solid line) and Hebi station (blue dotted line), and (c) zonal average hourly precipitation at 112°E–114.5°E.

northern Qinghai–Xizang Plateau and extended eastward to the eastern part of northwest China. A subtropical high system with strong intensity was located to the north, and the ridgeline affected eastern Liaoning Province. Meanwhile, a low-pressure system existed southeast of the continental high, corresponding to a cold vortex at 200 hPa, which was conducive to weather stability. In these weather conditions, the Huang-Huai area was located in an area of low pressure between the two anticyclones, and cyclonic vortices formed in the lower troposphere. From 1200 UTC July 19 to 1200 UTC July 21, the continental high moved westward then turned eastward. Simultaneously, “In-Fa” and “Cempaka” were westbound when the mid-latitude trough contracted eastward. Because of the stable weather conditions, the vortex remained in the Huang-Huai area for four consecutive days (Fig. 2(b)).

A large area of positive vorticity existed at 850 hPa in the middle and lower troposphere in western Henan at 0000 UTC on 20 July. The mesoscale vortex was strong and located south of the jet, along with a northeast–southwest shear line in central and northern Henan (Fig. 2(c)). In combination with the topographic distribution shown in Fig. 2(d), the northeast–southwest Taihang Mountains and the east-west Funiu Mountain present a unique horn-mouth shape, which the jet stream flows into before meeting a topographic barrier, developing a deep wind convergence in front of the mountain; this process helps maintain the vertical ascent and long duration of heavy rainfall.

The 925-hPa water vapor flux and 500-hPa potential height field are shown in Fig. 2(d). The “In-Fa” system developed into a severe typhoon at 0000 UTC on July 20 and interacted with the subtropical high, with the pressure gradient between them increasing rapidly. The easterly jet on the southern side of the subtropical high and northern side of the typhoon transported water vapor to Henan. The southeast jet controlled weather over the Henan region for a long time and supplied abundant water vapor for rainstorms. The water vapor flux then increased as the system encountered the topography of Taihang Mountain and Fu-niu Mountain, triggering an ascending motion.

In summary, upper tropospheric cold vortex, subtropical high, binary typhoons, middle-low vortex, and jet streams in the lower troposphere were the major weather systems influencing the development and continuation of extreme precipitation in Henan. The ability of a numerical model to characterize weather predictability directly determines the forecast accuracy of weather flow patterns, water vapor transport, and

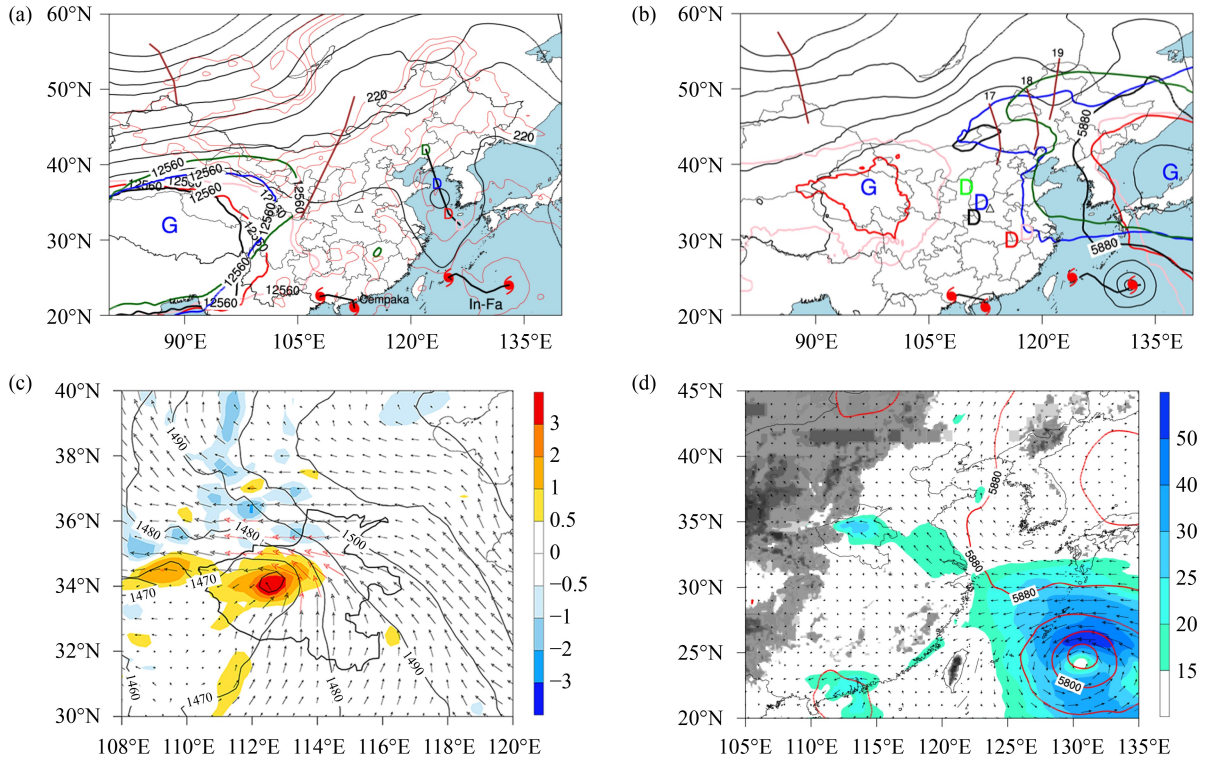

Fig. 2 Height fields of (a) 200 hPa and (b) 500 hPa at 1200 UTC on July 19, 2021, and evolution of the weather system from 1200 UTC on July 17 to 1200 UTC on July 21. Solid black lines denote contour lines, solid red lines are isotherms, and solid brown lines represent troughs. Pink, red, black, blue, and green lines denote the high pressure range at 1200 UTC on July 17, 18, 19, 20, and 21, respectively. D (G) represents the center of low (high) pressure, and △ represents Zhengzhou Station. (c) 850 hPa vorticity (color shadow, unit: 10^{-4} s^{-1}), geopotential height (black contour, units: gpm), and wind vector (red arrows represent wind speeds greater than 12 $m \cdot s^{-1}$, units: $m \cdot s^{-1}$). (d) 925 hPa water vapor flux (color shadow, unit: $cm \cdot s^{-1} \cdot hPa^{-1}$), 500 hPa geopotential height (red contour, unit: gpm), and terrain (gray shadow) at 0000 UTC on July 20, 2021.

convective intensity, which therefore affects the quality of precipitation intensity, location, and duration forecasts.

4 Predictability of the main weather system for GRAPES-REPS

4.1 Upper tropospheric cold vortex

At 0000 UTC on 20 July, an obvious upper tropospheric divergence occurred in central-eastern Henan, which was related to the upper-level outflow in the northeast and southwest airflow over the Hetao Plain. This upper-level outflow converged with the southwest jet on the west side of the cold vortex in the upper troposphere, forming the main upper tropospheric outflow, which was crucial for maintaining and enhancing the large-scale divergence over Henan (Fig. 3(a)). As shown by the 200-hPa circulation from GRAPES-REPS (Fig. 3(b)), the forecasted divergence over Henan was weaker than the observed divergence, and the large-value center was forecast further to the north, which may be one of the reasons for the more northward rainfall forecast. The intensity of the cold vortex was lower than the actual vortex intensity without the occurrence of a low-pressure center, and the forecasted northwest flow to the west of the cold vortex was weak.

By analyzing the relative vorticity and zonal mean of the horizontal wind field evolution at 200 hPa (Fig. 3(c)), we observed that the cold vortex center was located in the upper troposphere near 125°E from July 19 to 21, moving slowly eastward. After 19 July, the cold vortex in the upper troposphere increased rapidly and the jet streams strengthened accordingly, particularly on the west side of the vortex. The upper tropospheric divergence between 113°E and 117°E at 200 hPa and the vertical motion in the lower layer over Henan were synchronously enhanced. The upper tropospheric outflow over the heavy rain area converged with the western jet of the tropospheric cold vortex, and the upwelling at 850 hPa was quasi-stationary near Zhengzhou Station, forming a clear coupling with the upper tropospheric divergent flow. Such long-term dynamic conditions may be an important cause of the extreme precipitation in Henan. We comparing the ensemble mean with the actual value (Fig. 3(d)), it showed that the modeled divergence intensity over the heavy rain area in Henan was weaker than the actual divergence intensity at 0000 UTC on 20 July. Moreover, the modeled cold vortex intensity in the upper troposphere, jet streams, and vertical motion at 850

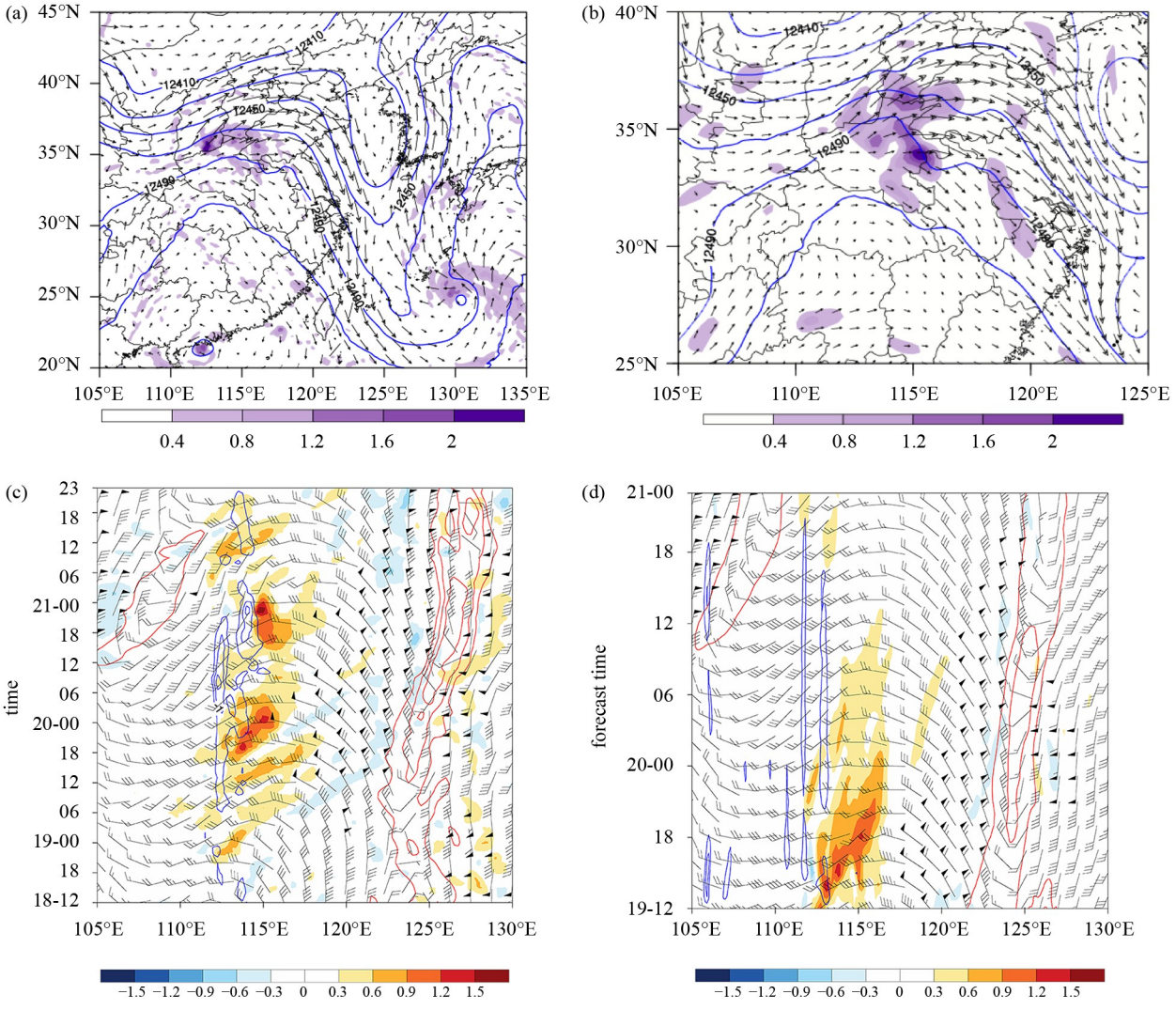

Fig. 3 (a, b) Geopotential height (solid blue line, units: gpm), wind vector (units: m·s^{-1}), and horizontal divergence (shadow, unit: 10^{-4} s^{-1}) at 200 hPa at 0000 UTC on July 20, 2021. (c, d) Temporal evolution of the zonal average (33°N–36°N) wind fields (wind barb), horizontal divergence (shadow, unit: 10^{-4} s^{-1}), relative vorticity (solid read line, $\geqslant 1\times10^{-4}$ s^{-1}) at 200 hPa and vertical velocity (solid blue line, $\leqslant -0.5$ pa·s^{-1}) at 850 hPa. (a, c) ERA5, (b, d) ensemble mean.

hPa were all weaker than the actual conditions, and the large-value center was shifted to the west.

The influence of the upper tropospheric cold vortex was further analyzed by classifying and comparing the ensemble members. Taking the average relative vorticity near the center of the upper tropospheric cold vortex at 0000 UTC on July 20 as a standard, we calculated the relative vorticity anomalies of the upper tropospheric cold vortex regions (30°N–40°N, 120°E–130°E) for each member (Fig. 4(a)), with member 9 (mem09) and member 10 (mem10) representing the optimal and the worst members, respectively. This is almost consistent with the result classified by the precipitation score (figure omitted). As shown in Figs. 4(b) and 4(c), the upper tropospheric cold vortex intensity of the optimal member was higher than that of the worst member, and the divergence was stronger over the Hetao Plain. Moreover, the ridge near the Hetao Plain was northerly, which was beneficial for enhancing the divergence outflow over Henan. At the same time, cold vortex circulation and divergence near the tropopause were stronger for the optimal member, with a larger vertical velocity in the lower layer, and coupling of the lower and upper troposphere was conducive to more accurate precipitation forecasting.

4.2 Vortex

According to the zonal section (34.7°N) of Zhengzhou (Fig. 5(a)), the positive relative vorticity region of the upper tropospheric cold circulation near 125°E was located at 300–150 hPa, and a steady easterly jet existed in the lower troposphere. An obvious convergence area was observed below 600 hPa, and a mesoscale vortex system corresponded to the positive relative vorticity near Zhengzhou, which further enhanced water vapor

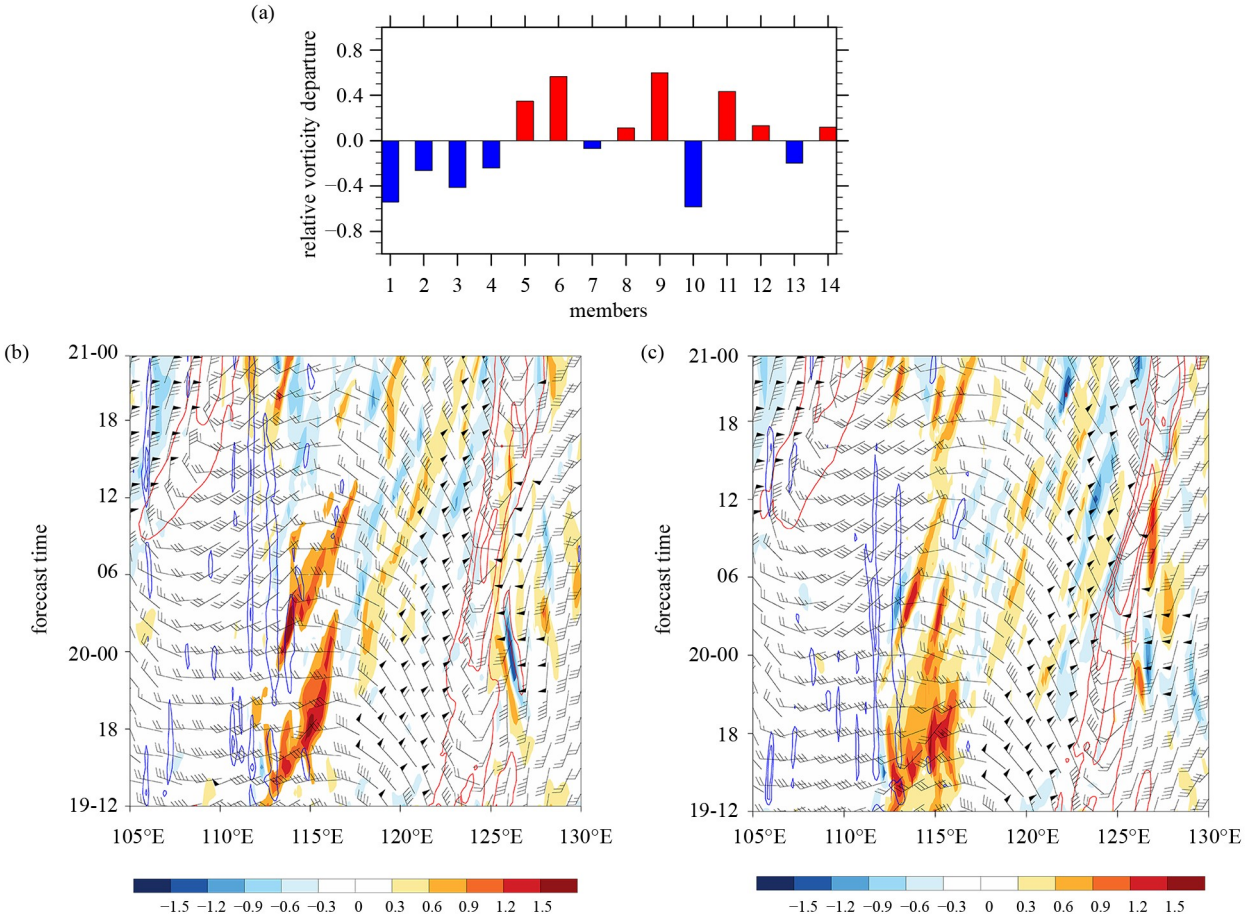

Fig. 4 (a) Relative vorticity anomalies (units: 10^{-5} s^{-1}) at 200 hPa of the regional average (30°N–40°N, 120°E–130°E) of the GRAPES-REPS ensemble mean at 0000 UTC on July 20, 2021, and temporal evolution of the zonal average (33°N–36°N) 200-hPa wind fields (wind barb), horizontal divergence (shadow, unit: 10^{-4} s^{-1}), relative vorticity (solid red lines, $\geqslant 1\times10^{-4}$ s^{-1}) and 850-hPa vertical velocity (solid blue lines, $\leqslant -0.5$ pa·s^{-1}) for (b) the optimal member (mem09) and (c) the worst member (mem10).

accumulation and convective organization, with strong convective upwelling extending over 200 hPa. A strong divergence occurred above 500 hPa over the heavy rain area, in which the westerly outflow converged with the jet on the west side of the upper tropospheric cold vortex near 200 hPa, establishing a coupling between convergence and uplift of the lower easterly jet and divergence and outflow of the upper northwesterly jet, leading to long-term heavy precipitation in central Henan.

The low vortex convergence, ascending motion, and divergence center intensity predicted by GRAPES-REPS were all weaker than the actual conditions (Figs. 5(a) and 5(b)), and the predicted divergence located at 400 hPa was lower than the actual divergence, directly underestimating the precipitation. Compared to the mean vorticity with the CAPE (Convective Available Potential Energy) value at 850 hPa (Figs. 5(c) and 5(d)), the vortex intensity forecast was weaker and the CAPE value was smaller, with some deviation from the actual value.

Based on the mean vorticity of each member at 850 hPa, the relative vorticity anomaly of each member indicates that the vortex intensity of the optimal member (mem09) was stronger than that of the worst member (mem10) (Fig. 6(a)) at 0000 UTC on 20 July. Compared with the zonal mean vorticity and the CAPE value, the vortex intensity and position for the optimal member (Fig. 6(b)) from 0000 to 1200 UTC were closer to the real situation, whereas the same values for the worst member (Fig. 6(c)) were significantly lower and located one longitude to the west, respectively. The optimal and worst members exhibited a slight difference in the CAPE value, whereas the large-value area of the optimal member was simulated closer to the real situation, particularly coinciding with the vortex at 850 hPa. In short, the optimal member has a better combination of instability and dynamic conditions in the lower layer.

4.3 Low-level jet stream

The low-level jet transported a large amount of heat and moisture for the extreme weather event, increasing the vertical wind shear, enhancing instability, and very strongly triggering and maintaining precipitation. The distributions of actual precipitation, wind fields at 925 hPa, and vorticity fields at 850 hPa (Figs. 7(a)–7(c)) show that the precipitation area was closely related to the

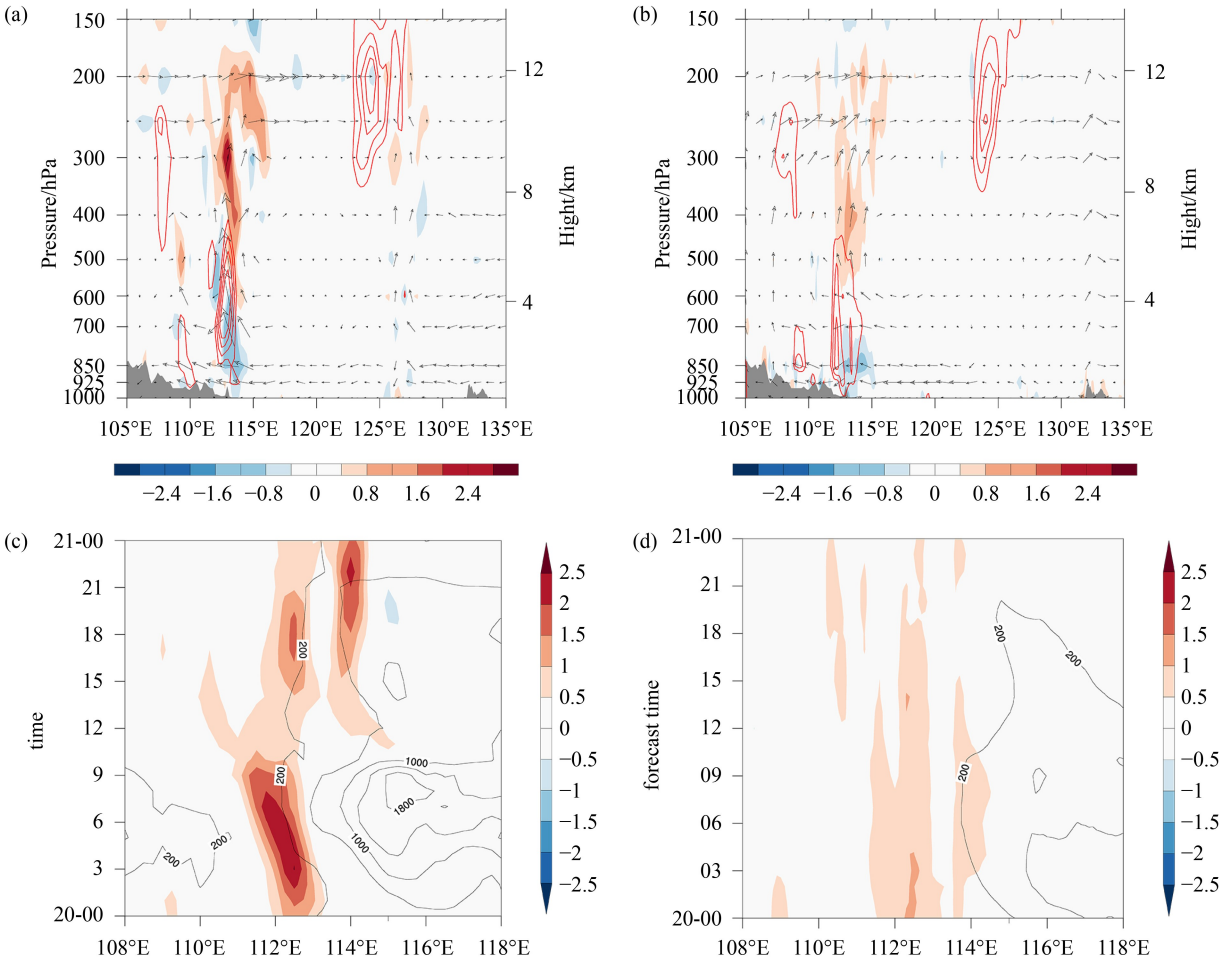

Fig. 5 (a, b) Vertical profile of divergence (shadow, unit: 10^{-4} s^{-1}), relative vorticity (red contour, $\geqslant 1\times10^{-4}$ s^{-1}), wind vector (arrow, units: $m\cdot s^{-1}$) and topography (gray shadow) along 34.7°N at 0000 UTC on July 20, 2021. (c, d) Temporal evolution of vorticity (shadow, unit: 10^{-4} s^{-1}) and CAPE (contours, units: $J\cdot kg^{-1}$) for the zonal average (34°N–36°N) at 850 hPa. (a, c) ERA5, (b, d) ensemble mean.

location of the boundary layer jet stream and the vorticity maximum center. In addition, the precipitation center was located near the jet stream and was directly affected by the movement and intensity changes of the vortex and jet zone. From 1200 UTC on July 19 to 2400 UTC on July 21, the jet stream gradually moved to the northeast and the southerly wind component increased, while the actual rain belt gradually moved to the northeast. The jet predicted by GRAPES-REPS from 1200 to 0000 UTC on July 19 was significant (Fig. 7(d)), and the location and intensity were relatively consistent with the actual situation, as was the vortex, resulting in a better precipitation forecast on 19 July. From 0000 UTC on July 20 to 0000 UTC on July 21 (Fig. 7(e)), the model forecast showed that the southerly wind component increased continuously. However, the intensity of the vortex varied minimally, and its location moved northward with the precipitation center. As expected, the simulation of precipitation intensity was not ideal. Up to 0000 UTC on July 22 (Fig. 7(f)), the southerly wind strengthened further, the jet stream intensity and vortex weakened, and the precipitation center of the model forecast moved to the northeast; however, the difference between the forecasted and observed rainfall intensity widened further, confirming that precipitation was closely related to the location and intensity of the boundary layer jet and vortex.

As shown in Fig. 8(a), an easterly jet appeared in the middle of Henan at 0000 UTC on July 20, and the zonal average precipitation area was closely related to the jet center shown in the distribution of the 925-hPa wind vector. From 0000 to 1200 UTC, the jet center and rain area were concentrated at 112°E–114°E, after which the jet center moved eastward along with the rain area. The precipitation distribution and 925-hPa wind vector of the ensemble mean (Fig. 8(b)) and the worst member (Fig. 8(d)) showed that the rain area was located one longitude to the east at 0000–0300 UTC on July 20, as was the jet position. As a result, precipitation abated and deviated from the observations. Because the jet stream moved to the west, the rainbands of the optimal member (Fig. 8(c)) gradually moved westward from 0000 UTC to 0900 UTC

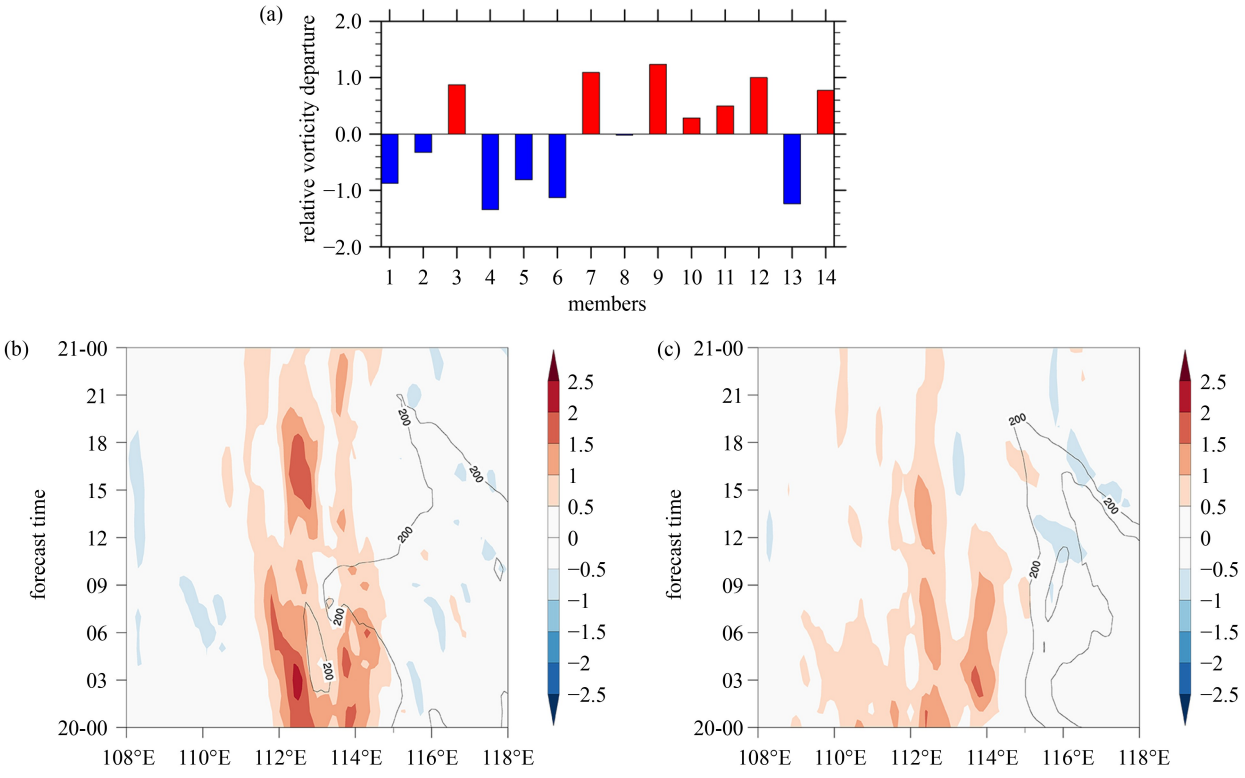

Fig. 6 (a) Relative vorticity anomalies (units: 10^{-5} s^{-1}) at 850 hPa of the regional average (33°N–39°N, 108°E–118°E) of the GRAPES-REPS ensemble mean at 0000 UTC on July 20, 2021, and temporal evolution of the zonal average (34°N–36°N) relative vorticity (units: 10^{-4} s^{-1}) and CAPE (solid line, units: $J \cdot kg^{-1}$) for (b) the optimal member (mem09) and (c) the worst member (mem10).

on July 20 and were concentrated in front of the mountain (112°E). The jet centers of the optimal member were maintained for a long time, resulting in a larger rainfall intensity than that of the worst member and the ensemble mean.

5 Ensemble prediction sensitivity analysis

5.1 Ensemble forecast sensitivity

Taking the regional average precipitation in the area of interest (34°E–38°E, 112°E–116°E) from 0000 to 1200 UTC on July 20 as the prediction objective function, we obtained the ensemble forecast sensitivity of the 200-hPa potential height field as the key prediction factor. At 0000 UTC on July 20, the highly sensitive area was located near the short-wave trough over the Hetao Plain, the cold vortex near Huang-Huai, the high-pressure ridge, and the upper troposphere around 105°E. Therefore, forecasted precipitation in the key regions had a high correlation with the intensity of the short-wave trough and the high-altitude cold vortex (Fig. 9(a)). When the deep short-wave trough in Hetao was to the east, the amplitudes of the Huang-Huai high-pressure ridge and the upper tropospheric cold vortex were larger, resulting in a more accurate prediction by the regional ensemble forecast system in the key precipitation regions. Taking the 850-hPa potential height as the forecast factor, the high-forecast sensitive area was located in the low vortex area, and the precipitation in the key area was more sensitive to low vortex intensity. When the vortex intensity was higher, low-level convergence and ascending motion were strengthened, increasing the strength of the convective system, which was conducive to more accurate precipitation forecasts (Fig. 9(b)).

When the factors were selected as the meridional wind at 850 hPa and 925 hPa, the high forecast sensitivity area coincided with the jet stream (Fig. 10), and the precipitation forecast was highly sensitive to the meridional wind intensity. The stronger the southern wind in this area, the heavier the rainfall intensity in the key area. Meanwhile, the sensitivity range of the 925-hPa meridional wind as a forecast factor was larger than that of the 850-hPa meridional wind. The above analysis shows that the precipitation forecast was highly sensitive to the low-level jet. However, compared with the low-level jet at 850 hPa, the boundary layer jet had a larger positive effect on precipitation.

5.2 Heavy precipitation forecast performance

Figures 11(a) and 11(b) show the 24-h ensemble mean cumulative precipitation and the spread of precipitation

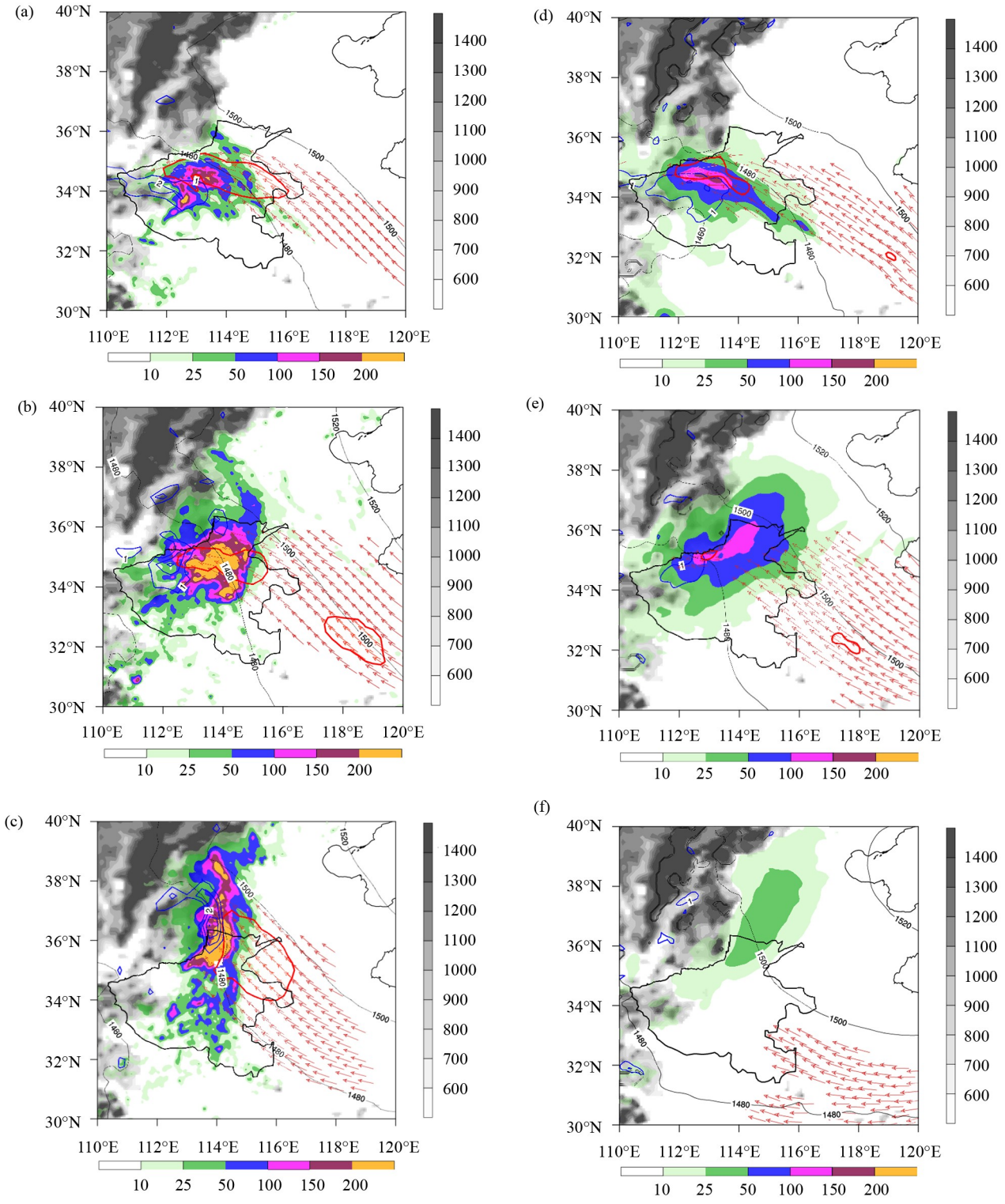

Fig. 7 24-h Cumulative precipitation (color, units: mm), wind speed ⩾10 m·s^{-1} (red arrow), and ⩾12 m·s^{-1} (red contour) at 925 hPa, 850-hPa height (black line, units: gpm), relative vorticity (blue line, ⩾1×10^{-4} s^{-1}), and terrain height (gray shadow, units: m). (a, d) 0000 UTC on July 20, (b, e) 0000 UTC on July 21, (c, f) 0000 UTC on July 22. (a, b, c) the precipitation data of CMORPH, and wind, height and relative vorticity of ERA5; (d, e, f) ensemble mean of GRAPES-REPS.

predicted by GRAPES-REPS and ECMWF-EPS, respectively. The large-value area of precipitation predicted by GRAPES-REPS was located in north-central Henan with low rainfall intensity. Compared to the observations, the precipitation area was further to the north. Area with precipitation spread exceeding 40 mm

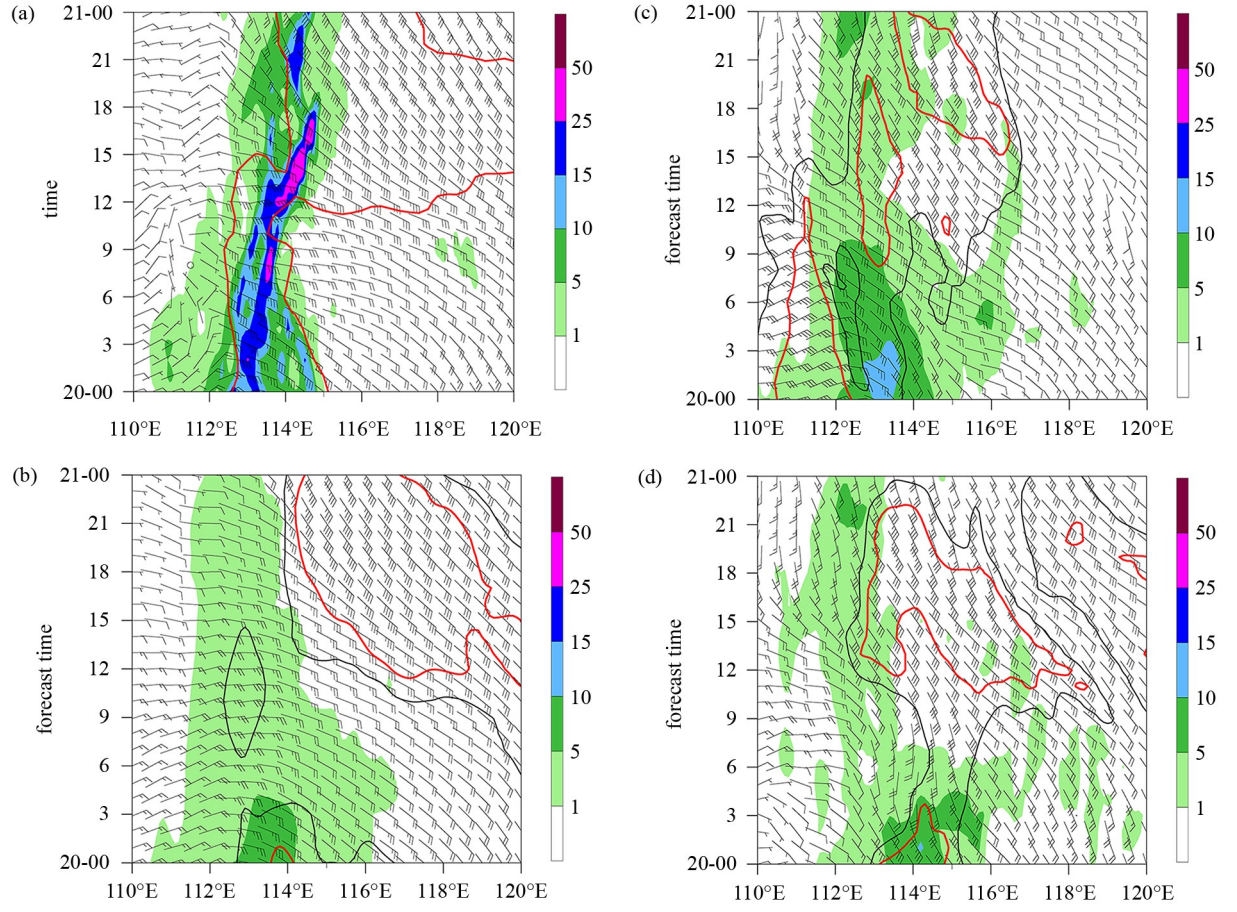

Fig. 8 Temporal evolution of the zonal average (34°N–35°N) precipitation (shadow, units: mm) and 925-hPa wind vector (units: m·s^{-1}) from 0000 to 2400 UTC on July 20, 2021. Red and black contours denote wind speeds of 12 m·s^{-1} and 10 m·s^{-1}, respectively. (a) ERA5, (b) ensemble mean, (c) optimal member, (d) worst member.

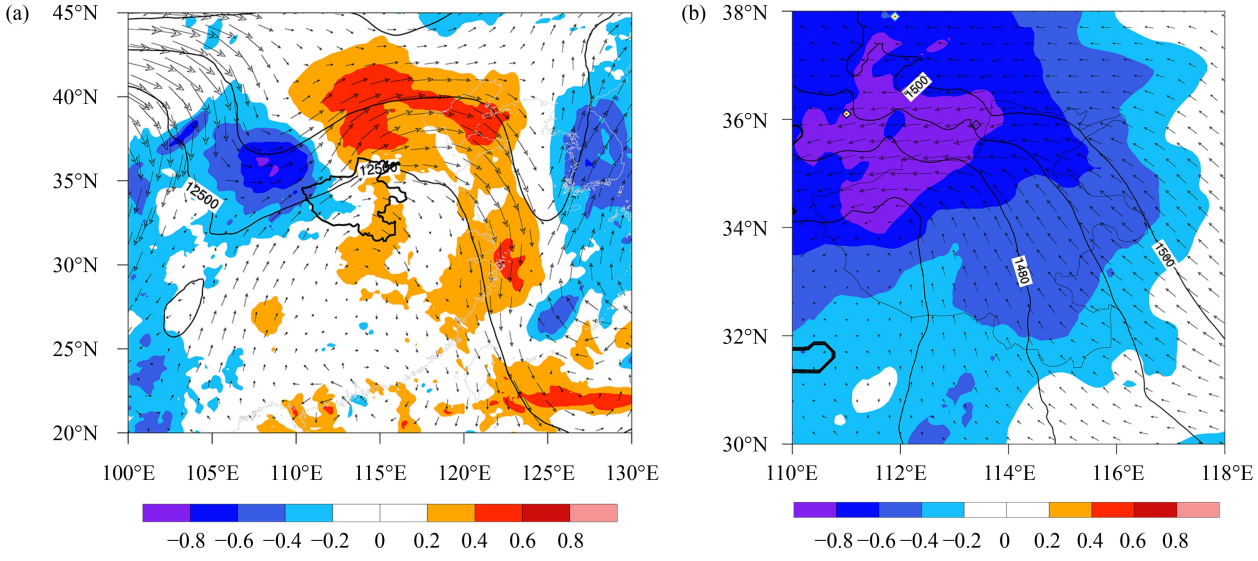

Fig. 9 Wind fields (arrow, units: m·s^{-1}), potential height (line, units: gpm) of ensemble mean, and ensemble sensitivity of the potential height to mean precipitation for key areas (shadow) at 0000 UTC on July 20, 2021. (a) 200 hPa, (b) 850 hPa.

was located in the northeast of Henan, which coincided with the low-level jet stream and upper-level cold vortex, indicating that the precipitation forecast was affected by strong weather systems such as low-level jet streams and upper tropospheric cold vortices. The precipitation area of the ECMWF-EPS ensemble mean was further to the west

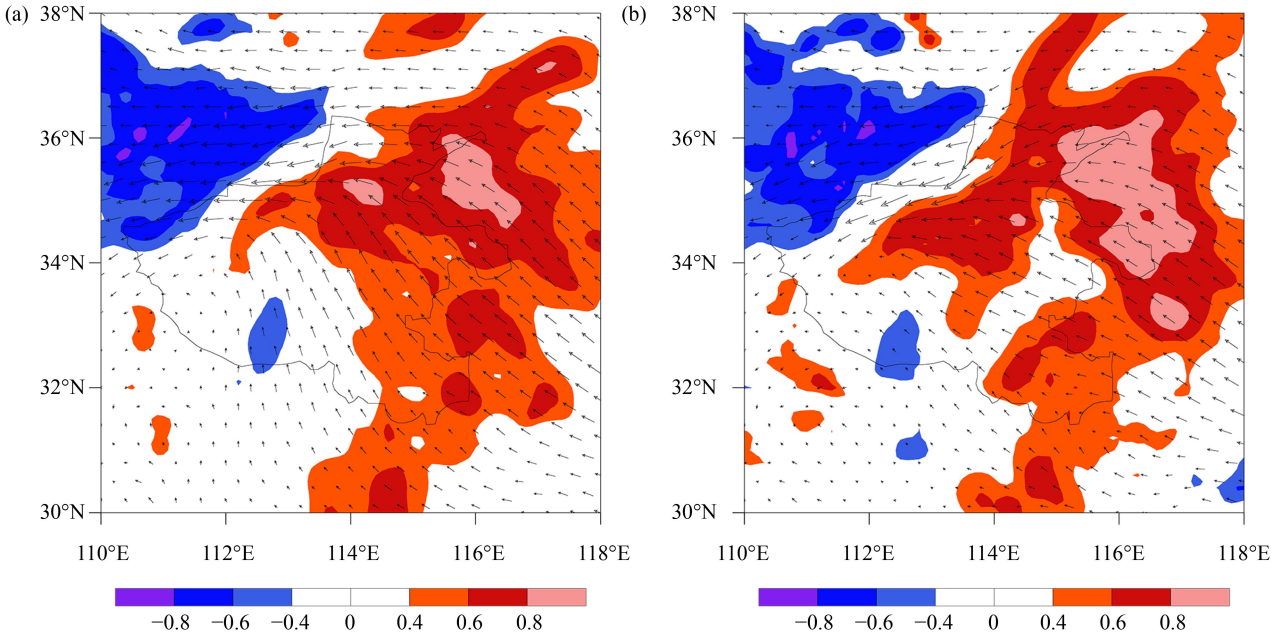

Fig. 10 Wind fields (arrow, units: $m \cdot s^{-1}$) of the ensemble mean and ensemble sensitivity of the meridional wind to mean precipitation in the key area (shadow) at 0000 UTC on July 20, 2021. (a) 850 hPa, (b) 925 hPa.

than the actual precipitation area, and the large precipitation dispersal area deviated from the actual precipitation center with low rainfall intensity. The probability distribution of cumulative precipitation greater than 50 mm (Figs. 11(c) and 11(d)) and 100 mm (Figs. 11(e) and 11(f)) showed that most members of GRAPES-REPS could successfully predict precipitation along the Taihang Mountain, corresponding to the large-value area of precipitation probability. This indicated that GRAPES-REPS has high predictability for heavy precipitation caused by topography. The difference between ECMWF-EPS and GRAPES-REPS was smaller in the heavy rainfall probability forecast; however, GRAPES-REPS had obvious advantages in magnitude and range, showing consistency with the distribution of precipitation along topography. In conclusion, GRAPES-REPS showed a better forecast performance than ECMWF-EPS, especially because some members of GRAPES-REPS effectively simulate extreme precipitation.

At 0000 UTC on July 20, a fast-growing low vortex and low-level jet emerged in the lower troposphere of the north-western Henan Province. Compared to the actual conditions (Fig. 2(c)), the low vortex and the low-level jet predicted by GRAPES-REPS were further to the north and the intensity of the low vortex was weaker than that of the actual vortex (Fig. 12(a)). The low vortex predicted by ECMWF-EPS was located to the north and its intensity was lower than that of GRAPES-REPS (Fig. 12(b)). The moving path of the low vortex (Fig. 12(c)) indicates that the actual low vortex (black solid line) moved northwestward from July 20, and turned abruptly to the southeast at 0900 UTC, and turned to the northeast at 1500 UTC. Compared to the ECMWF-EPS, the moving path of the low vortex predicted by GRAPES-REPS was simulated closer to the real situation and the intensity was always higher. Although ECMWF-EPS forecast the movement of the low vortex to the north-west, the low vortex was located in the north-west of Henan Province for a long time. The deviation of the low vortex position was obviously larger than that of GRAPES-REPS, which make the rainfall forecast northward. In short, more accurate descriptions of the critical weather systems were provided in GRAPES-REPS, leading to more accurate precipitation forecasts.

6 Discussion

According to the synoptic characteristics and key factors impacting the "7·20" extreme precipitation event in Henan, we applied the ensemble sensitivity method to investigate the causes and possible mechanisms affecting the predictability of various major weather systems during this extreme precipitation event. The main conclusions are as follows.

1) Multiple weather systems, including subtropical highs, continental highs, and typhoons, provided a stable circulation background for this weather event. The easterly jet between the subtropical high and Typhoon In-Fa continued to transport water vapor to northwestern Zhengzhou, and formed local strong convection under the influence of topographic uplift and mesoscale low vortices. Meanwhile, strong divergence of the upper troposphere in Henan was confluent with the jet streams on the west side of the cold vortex, constituting a

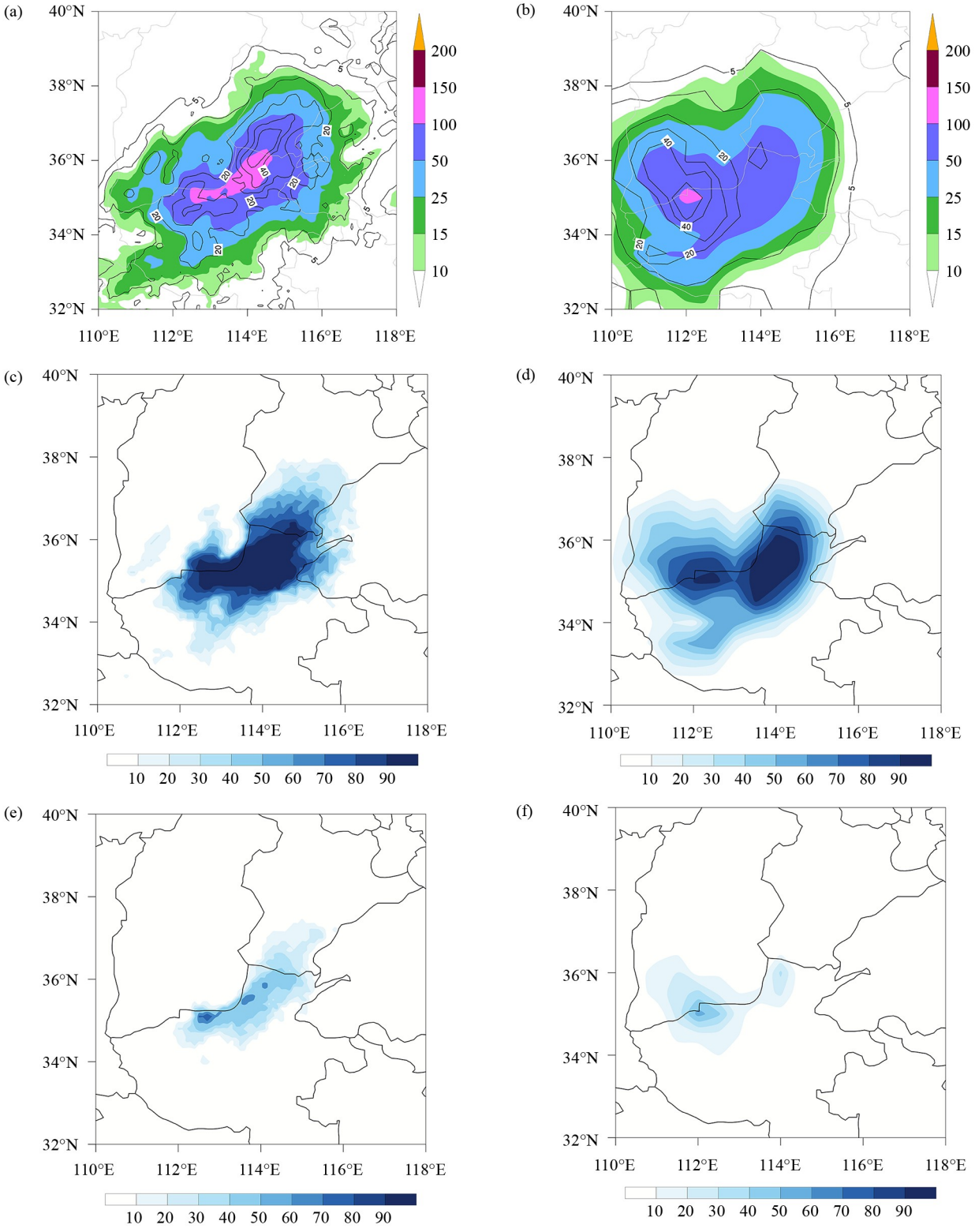

Fig. 11 (a, b) Ensemble mean precipitation (shadow, units: mm) and forecast precipitation dispersion (contour, units: mm); (c, d) forecast probability of precipitation ⩾50 mm and (e, f) forecast probability of precipitation ⩾100 mm from 0000 to 2400 UTC on July 20, 2021. (a, c, e) GRAPES-REPS, (b, d, f) ECMWF-EPS.

coupling of the lower and upper troposphere, which was conducive to the development and continuation of precipitation, prompting the extreme precipitation event to be heavier, more efficient, and longer lasting.

2) The intensity of the upper tropospheric cold vortex and the low-level vertical velocity simulated by the

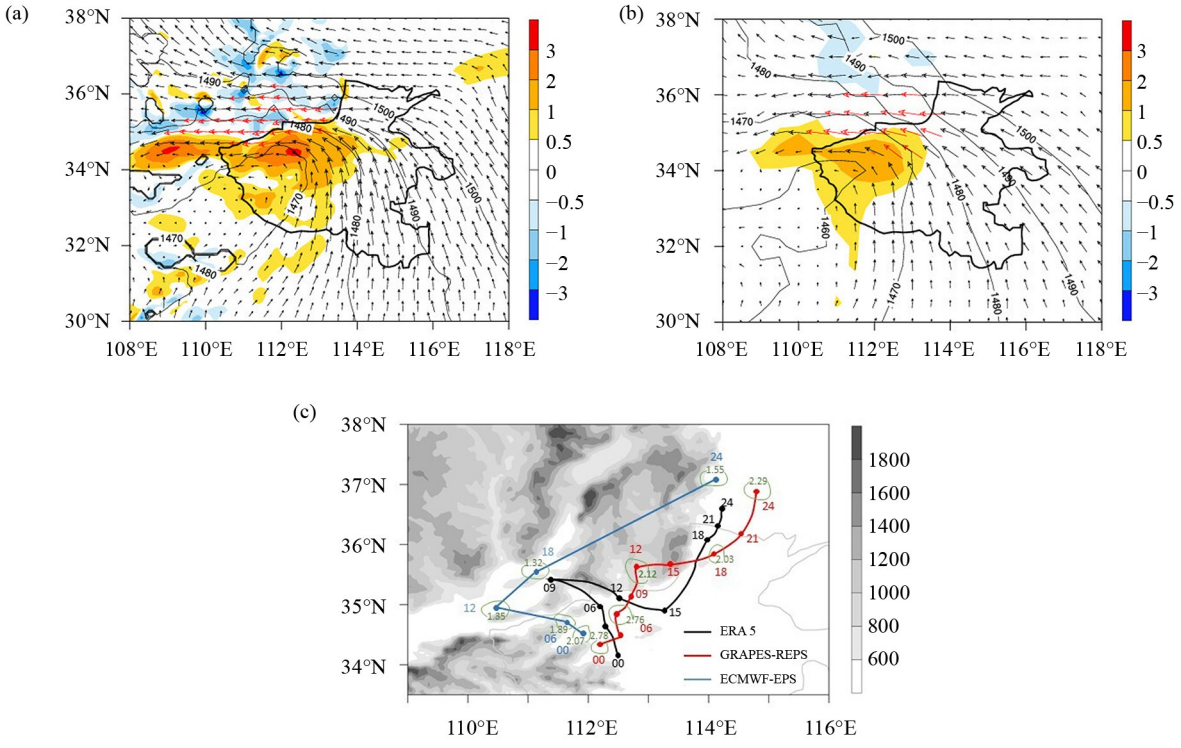

Fig. 12 850-hPa relative vorticity (color shadow, unit: 10^{-4} s^{-1}), geopotential height (black contour, units: gpm), and wind vector (red arrows represent wind speeds greater than 12 $m \cdot s^{-1}$, units: $m \cdot s^{-1}$) for (a) GRAPES-REPS ensemble mean and (b) ECMWF-EPS ensemble mean. (c) Low vortex moving paths of ERA5 (black solid line), GRAPES-REPS ensemble mean (red solid line, green contour denote relative vorticity, unit: 10^{-4} s^{-1}) and ECMWF-EPS ensemble mean (blue solid line) from 0000 to 2400 UTC on July 20, 2021 at 3-hour interval. The symbols 00, 06, 09, 12, 15, 18, 21, 24 denote 0000, 0600, 0900, 1200, 1500, 1800, 2100, 2400 UTC on 20 July, respectively. Gray shaded indicates terrain (unit: m).

optimal member were stronger than that of the worst member, resulting in closer coupling with the observations. Simultaneously, the intensity and location of the low vortex in the middle layer and the evolution characteristics of the unstable energy in the lower layer were described more accurately by the optimal than the worst member. Moreover, the coupling position predictions of the low-vortex and low-level jet streams were more accurate, and the meridional wind component of the jet stream was stronger. Compared with the optimal member, the instability and dynamic conditions of the worst member differed from the actual values, which resulted in an obvious deviation in precipitation intensity and area.

3) The intensities of the short-wave trough, upper tropospheric cold vortex, low vortex, and low-level jet stream had a higher ensemble sensitivity to heavy precipitation. The extreme precipitation event was more sensitive to the boundary layer jet than the low-level jet stream over 850 hPa, and a stronger boundary layer jet was helpful for predicting precipitation more accurately.

4) GRAPES-REPS has greater uncertainty in heavy precipitation forecasts caused by strong weather systems, such as low-level jet streams, but shows high predictability for heavy precipitation caused by topography. In contrast to ECMWF-EPS, GRAPES-REPS shows a better forecasting ability, with some ensemble members able to predict extreme precipitation events more effectively.

We employed GRAPES-REPS and used the means of comparison of members and ensemble sensitivity analysis to explore the dominant contributor affecting the predictability. The prediction ability of the optimal member of GRAPES-REPS was attributed to effective prediction of the intensity and evolution characteristics of the upper tropospheric cold vortex, middle-low vortex, and low-level jet. The influence of weather scale system on precipitation is compared in detail. At the same time, the effect of upper tropospheric cold vortex on precipitation is not mentioned in previous studies.

Many factors affect the predictability of heavy precipitation, especially during complex extreme weather events, which are expressed differently when the predictability of ensemble sensitivity analysis is constrained by the quality of the ensemble forecast. In future, higher-quality and higher-resolution ensemble forecasts could be employed to analyze the predictability of small-scale and mesoscale weather systems during the “7·20” extreme precipitation event in Henan, and more accurately characterize the occurrence, development, and predictability of severe convective weather systems. In addition, it is difficult to reflect the forecasting ability of GRAPES-REPS using only one extreme precipitation

event, which may differ from other effective weather systems in their precipitation characteristics and physical mechanisms.

Acknowledgments This study was supported by the National Natural Science Foundation of China (Grant No. U2242213) and the National Key R&D Program of China (No. 2017YFC1502000). We acknowledge the High Performance Computing Centre of the Nanjing University of Information Science & Technology for their support.

Competing interests The authors declare that they have no competing interests.

References

Buizza R, Miller M, Palmer T N (1999). Stochastic representation of model uncertainties in the ECMWF ensemble prediction system. Q J R Meteorol Soc, 125(560): 2887–2908

Chen G, Zhao K, Lu Y, Zheng Y, Xue M, Tan Z M, Xu X, Huang H, Chen H, Xu F, Yang J, Zhang S, Fan X (2022). Variability of microphysical characteristics in the "21·7" Henan extremely heavy rainfall event. Sci China Earth Sci, 65(10): 1861–1878

Chen J, Li X L (2020). The review of 10 years development of the GRAPES global/regional ensemble prediction. Adv Meteorol Sci Technol, 10(2): 9–18 (in Chinese)

Chen T, Sun J, Chen Y, Guo Y Q, Xu J (2019). Study on the numerical predictivity of localized severe mesoscale rainstorm in Guangzhou on 7 May 2017. Meteor Mon, 45(9): 1199–1212 (in Chinese)

Cholaw B, Zhuge A R, Xie Z W, Gao Z T, Lin D W (2022). Water vapor transportation features and key synoptic-scale systems of the "7·20" rainstorm in Henan province in 2021. Chin J Atmos Sci, 46(3): 725–744 (in Chinese)

Du J (2002). Present situation and prospects of ensemble numerical prediction. J Appl Meteorol Sci, 13(1): 16–28 (in Chinese)

Du Y, Chen G X (2018). Heavy rainfall associated with double low-level jets over Southern China. Part I: ensemble-based analysis. Mon Weather Rev, 146(11): 3827–3844

Gao L, Chen J, Zheng J W, Chen Q L (2019). Progress in researches on ensemble forecasting of extreme weather based on numerical models. Adv Earth Sci, 34(7): 706–716 (in Chinese)

Ji X D, Qi L B (2018). Evaluation and application of ECMWF model precipitation and extreme weather forecast index of precipitation on heavy rainfall forecast. Torrential Rain and Disasters, 37(6): 566–573 (in Chinese)

Jiang X M, Yuan H L, Xue M, Chen X, Tan X G (2014). Analysis of a torrential rainfall event over Beijing on 21–22 July 2012 based on high resolution model analyses and forecasts. Acta Meteorol Sin, 72(2): 207–219 (in Chinese)

Leith C S (1974). Theoretical skill of Monte Carlo forecast. Mon Weather Rev, 102(6): 409–418

Li H, Wang X M, Zhang X, Lv L Y, Xu W M (2018). Analysis on extremity and characteristics of the 19 July 2016 severe torrential rain in the north of Henan province. Meteor Mon, 44(9): 1136–1147 (in Chinese)

Lorenz E N (1963). Deterministic nonperiodic flow. J Atmos Sci, 20(2): 130–141

Lorenz E N (1969). The predictability of a flow which possesses many scales of motion. Tellus, Ser A, Dyn Meterol Oceanogr, 21(3): 289–307

Ma X L, He P Y, Zhou B Y, He J (2021). Impact of localization of ensemble transform Kalman filter on initial perturbation of regional ensemble forecast. Trans Atmos Sci, 44(2): 314–323 (in Chinese)

Ma X L, Ji Y X, Zhou B Y, Shi Y, Li L L, Guo H (2018). A new scheme of blending initial perturbation of the GRAPES regional ensemble prediction system. Trans Atmos Sci 41(2): 248–257 (in Chinese)

Ma X L, Xue J S, Lu W S (2009). Study on ETKF-based initial perturbation scheme for GRAPES global ensemble prediction. Acta Meteorol Sin, 23(5): 562–574

Medina H, Tian D, Marin F R, Chirico G B (2019). Comparing GEFS, ECMWF, and postprocessing methods for ensemble precipitation forecasts over Brazil. J Hydrometeorol, 20(4): 773–790

Melhauser C, Zhang F Q (2012). Practical and intrinsic predictability of severe and convective weather at the mesoscales. J Atmos Sci, 69(11): 3350–3371

Pan X, Wang Q P, Zhang Y, He P Y, Ma X L (2021). Analysis constraints scheme of initial perturbation of ensemble prediction. Chin J Atmos Sci, 45(6): 1327–1344 (in Chinese)

Quandt L A, Keller J H, Martius O, Pinto J G, Jones S C (2019). Ensemble sensitivity analysis of the blocking system over Russia in summer 2010. Mon Weather Rev, 147(2): 657–675

Schumacher R S (2011). Ensemble-based analysis of factors leading to the development of a multiday warm-season heavy rain event. Mon Weather Rev, 139(9): 3016–3035

Sun J H, Zhao S X, Fu S M, Wang H J, Zheng L L (2013). Multi-scale characteristics of record heavy rainfall over Beijing area on July 21, 2012. Chin J Atmos Sci, 37(3): 705–718 (in Chinese)

Sun J, Chen Y, Yang S N, Dai K, Chen T, Yao R, Xu J (2012). Analysis and thinking on the extremes of the 21 July 2012 torrential rain in Beijing part II: preliminary causation analysis and thinking. Meteor Mon, 38(10): 1267–1277 (in Chinese)

Sun L, Chen S Y, Pan X, Wang Q P, He J, Ma X L (2022). Sensitivity analysis of model initial value of a rainstorm in the warm sector of South China. J Meteorol Sci, 42(3): 356–367 (in Chinese)

Torn R D, Hakim G J (2008). Ensemble-based sensitivity analysis. Mon Weather Rev, 136(2): 663–677

Wang J Z, Chen F J, Chen J, Liu X Q, Li H Q, Deng G, Li X L, Wang Y Z (2021). Verification of GRAPES-REPS model precipitation forecasts over China during 2019 flood season. Chin J Atmos Sci, 45(3): 664–682 (in Chinese)

Wei P, Xu X, Xue M, Zhang C Y, Wang Y, Zhao K, Zhou A, Zhang S S, Zhu K F (2023). On the key dynamical processes supporting the 21.7 Zhengzhou record-breaking hourly rainfall in China. Adv Atmos Sci, 40(3): 337–349

Wu M W, Luo Y L, Chen F, Wong W K (2019). Observed link of extreme hourly precipitation changes to urbanization over coastal South China. J Appl Meteorol Climatol, 58(8): 1799–1819

Xiao L S, Zhang H L, Zhang X B, Feng L, Chen Z G, Dai G F (2021). Predictability analysis of the extremely heavy rainfall in the Pearl River Delta on 22 May 2020 using CMA-TRAMS-based ensemble

prediction system. Acta Meteorol Sin, 79(6): 956–976 (in Chinese)

Xue J S, Liu Y (2007). Numerical weather prediction in China in the new century-progress, problems and prospects. Adv Atmos Sci, 24(6): 1099–1108

Yu H Z, Meng Z Y (2016). Key synoptic-scale features influencing the high impact heavy rainfall in Beijing, China, on 21 July 2012. Tellus A: Dyn Meteorol Oceanogr, 68(1): 31045

Yuan Y, Li X L, Chen J, Xia Y (2016). Stochastic parameterization toward model uncertainty for the GRAPES mesoscale ensemble prediction system. Meteor Mon, 42(10): 1161–1175 (in Chinese)

Zhang X B (2018a). A GRAPES-based mesoscale ensemble prediction system for tropical cyclone forecasting: configuration and performance. Q J R Meteorol Soc, 144(711): 478–498

Zhang X B (2018b). Application of a convection-permitting ensemble prediction system to quantitative precipitation forecasts over southern China: preliminary results during SCMREX. Q J R Meteorol Soc, 144(717): 2842–2862

Zhang X, Yang H, Wang X M, Shen L, Wang D, Li H (2021). Analysis on characteristic and abnormality of atmospheric circulations of the July 2021 extreme precipitation in Henan. Trans Atmos Sci, 44(5): 672–687 (in Chinese)

Zhang Y, Shi Y, Zhou B Y, Ma X L (2022a). Physical structures and evolution characteristics of wind perturbation in ensemble prediction. Trans Atmos Sci, 45(2): 268–279 (in Chinese)

Zhang Y, Yu H, Zhang M, Yang Y, Meng Z (2022b). Uncertainties and error growth in forecasting the record-breaking rainfall in Zhengzhou, Henan on 19–20 July 2021. Sci China Earth Sci, 65(10): 1903–1920

Zhu K F, Xue M (2016). Evaluation of WRF-based convection-permitting multi-physics ensemble forecasts over China for an extreme rainfall event on 21 July 2012 in Beijing. Adv Atmos Sci, 33(11): 1240–1258

Zhu K F, Zhang C Y, Xue M, Yang N (2022). Predictability and skill of convection-permitting ensemble forecast systems in predicting the record-breaking “21·7” extreme rainfall event in Henan Province, China. Sci China Earth Sci, 65(10): 1879–1902